Star Formation News Letter No. 343, #8-13：工藤哲洋

8. **SIRIUS Project. III. Star-by-star simulations of star cluster formation using a direct N-body integrator with stellar feedback**

Michiko S. Fujii, Takayuki R. Saitoh, Yutaka Hirai, Long Wang

(1) 9. **X-ray Super-Flares From Pre-Main Sequence Stars: Flare Modeling**

Konstantin V. Getman, Eric D. Feigelson, Gordon P. Garmire

(2) 10. **The Macroporosity of Rubble Pile Asteroid Ryugu and Implications for the Origin of Chondrules**

William Herbst, James P. Greenwood, Teng Ee Yap

11. **Misaligned Circumstellar Disks and Orbital Motion of the Young Binary XZ Tau**

Takanori Ichikawa, Miyu Kido, Daisuke Takaishi, Yoshito Shimajiri, Yusuke Tsukamoto, Shigehisa Takakuwa

(3) 12. **ALMA observations of doubly deuterated water: Inheritance of water from the prestellar environment**

S. S. Jensen, J. K. Jørgensen, L. E. Kristensen, A. Coutens, E. F. van Dishoeck, K. Furuya, D. Harsono, M. V. Persson

13. **A Deep Search for Five Molecules in the 49 Ceti Debris Disk**

Jessica Klusmeyer, A. Meredith Hughes, Luca Matra, Kevin Flaherty, Agnes Kospal, Attila Moor, Aki Roberge, Karin Oberg, Aaron Boley, Jacob White, David Wilner, Peter Abraham

（1）

9. X-ray Super-Flares From Pre-Main Sequence Stars: Flare Modeling

Konstantin V. Getman, Eric D. Feigelson, Gordon P. Garmire

◆前主系列星のスパーフレアのX線観測とモデルとの比較から，フレアの温度やループサイズなどを調べてカタログを作成し，統計的な解析を行った.

◆Chandra衛星が観測した1086個のスーパーフレアから，明るい55個を選んで調べた：

質量 $0.2M_{\odot} - 18M_{\odot}$，円盤あり＋円盤なしを含む

◆太陽フレアや，主系列星フレアとも比較した.

⬇

◆フレアの性質は，円盤のあるなしには関係がなかった.
太陽フレア（コロナ質量放出を伴う）と同じモデルで説明できそうである.

◆エネルギーの大きさ（など）と星の質量とに相関があった.

◆磁束とフレア光度との相関が，太陽フレアよりやや急

フレアの磁気リコネクションモデル
（天文学辞典より）

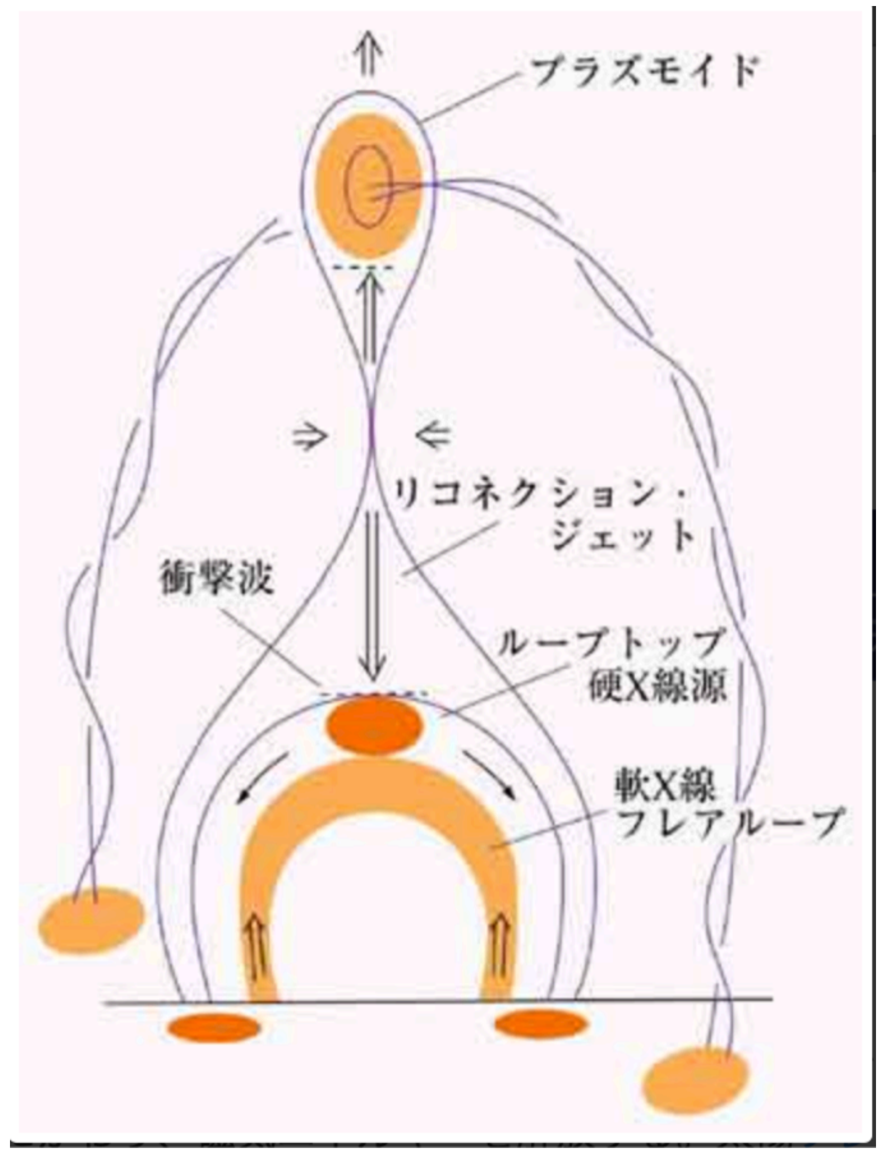

原始星フレアのモデル

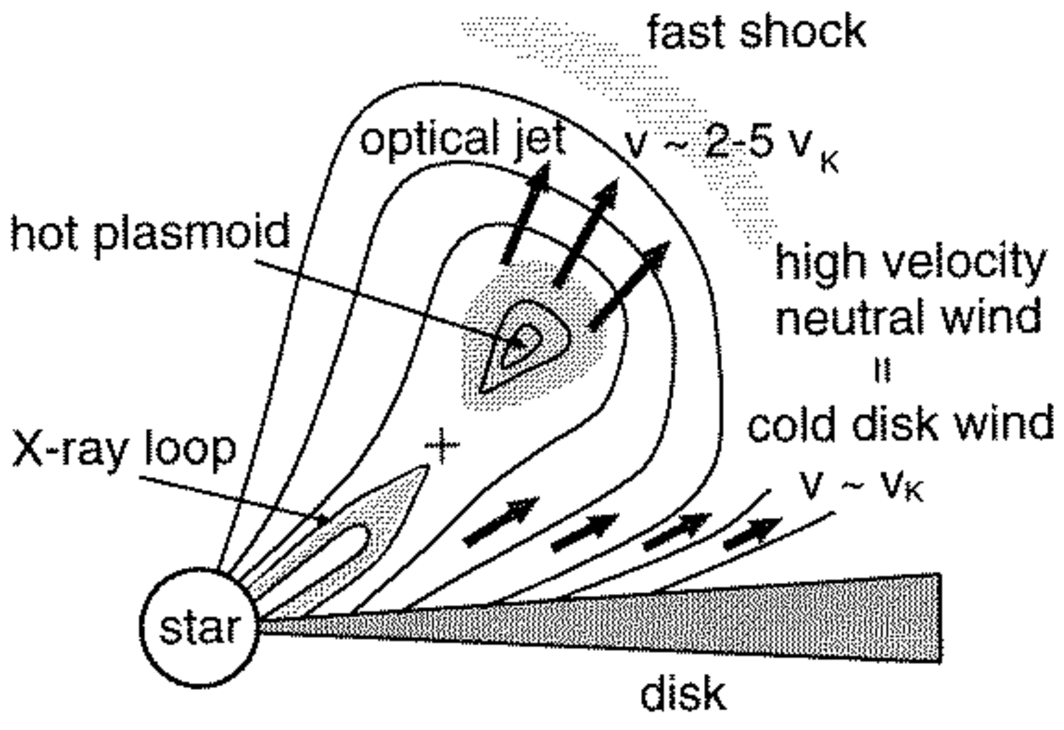

(Hayashi, Matsumoto, Shibata 1996)

方法

観測されたスーパーフレア星の，質量，半径，フレアエネルギーの累積頻度分布

緑：光子数＞1000：55個 （この論文で解析した星）

赤：光子数＜1000：1031個

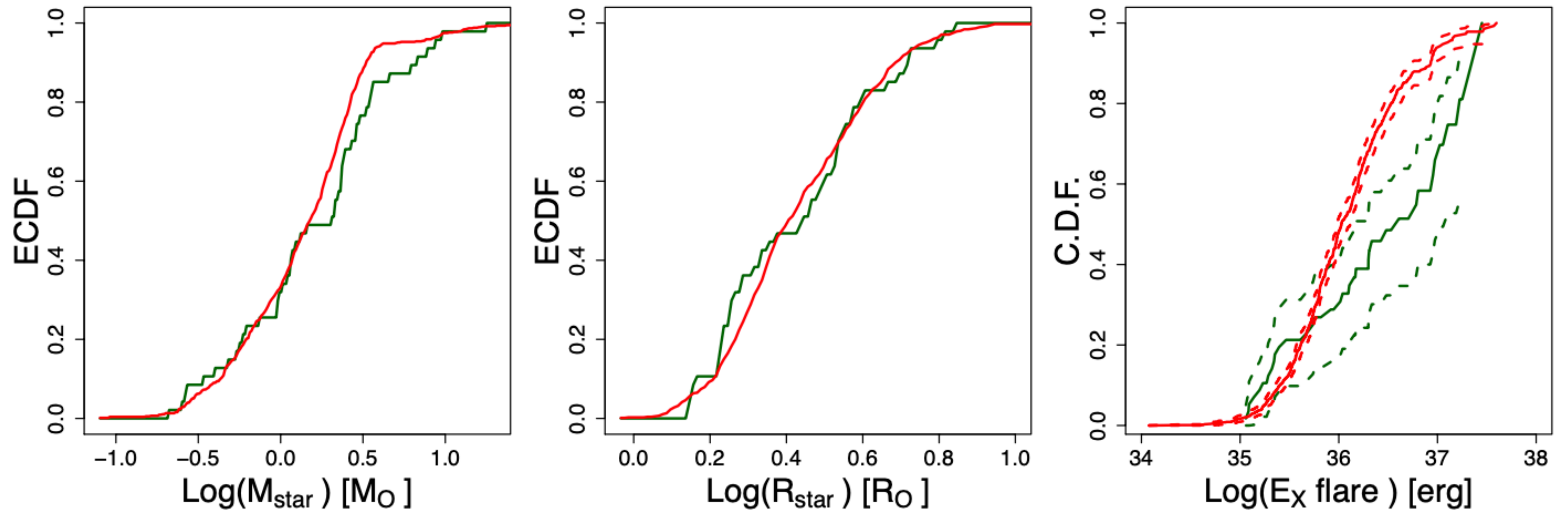

Figure 1. Cumulative distribution functions of the X-ray flare host stellar mass (left), stellar radius (middle), and flare energy integrated from the start to the stop time (right). The latter is constructed using Kaplan-Meier survival estimators for 'R' and 'D' flares with the dashed curves representing 95% confidence bands (see Paper I for details). The MYStIX/SFiNCs super-flares are stratified by brightness: the green curve shows the 55 events associated with > 1000-photon *Chandra* observations (studied here) while the red curve shows the 1,031 remaining events associated with < 1000-photon observations.

解析したフレアの一例

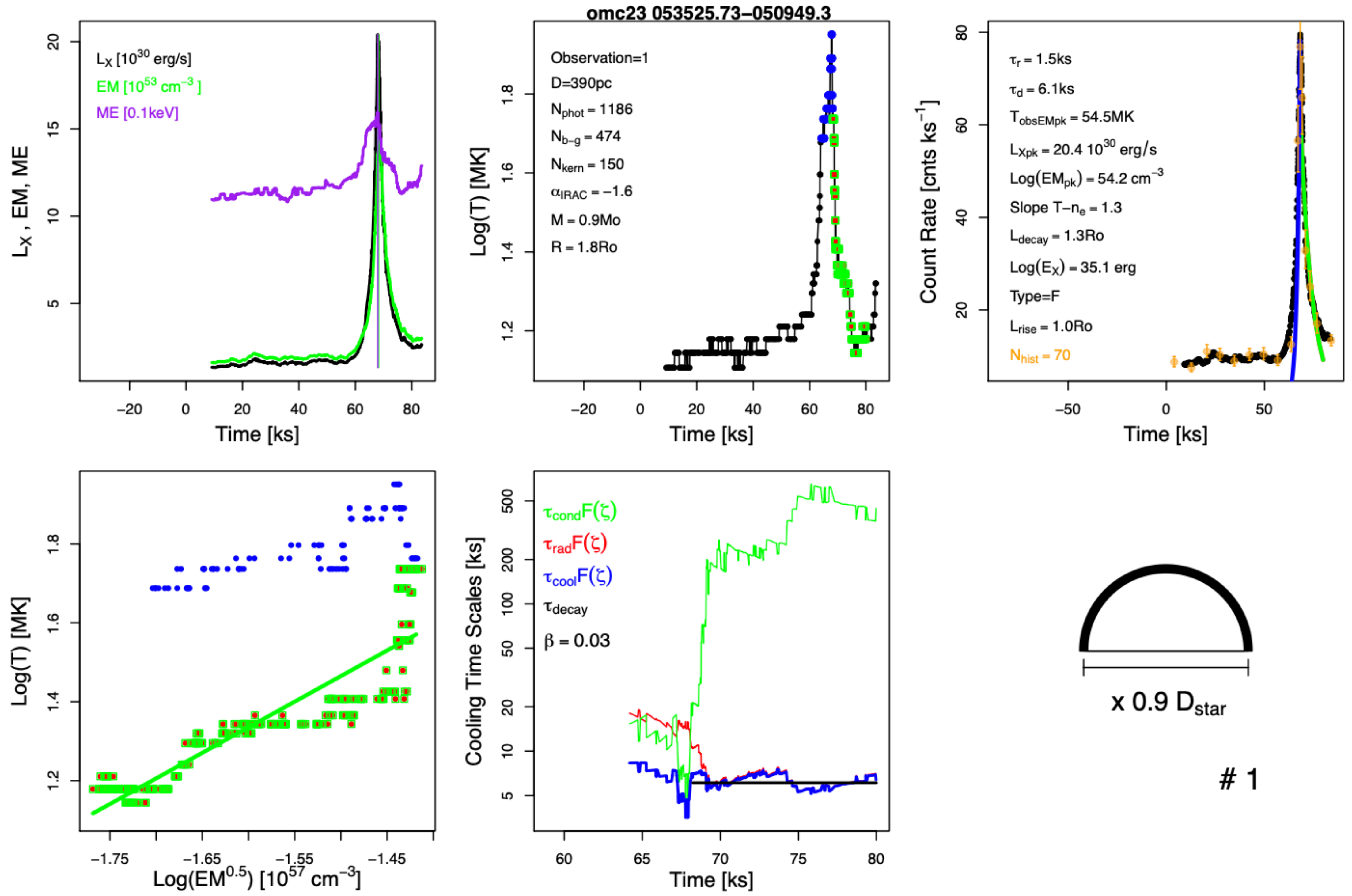

Figure 2. Sample page from the MYStIX/SFiNCs super-flare atlas. See §2.2 for explanations of the figures and legends. The complete figure set for 55 super flares is available in the electronic article.

Table 1. Fifty Five Bright MYStIX/SFiNCs X-ray Super-flares

Host Star Properties				Super-flare Properties									
MYStIX/SFiNCs	M	R	α_{IRAC}	Type	τ_{rise}	τ_{decay}	$L_{X,pk}$	EM_{pk}	$T_{obs,pk}$	$T_{obs,EM}$	L_{decay}	L_{rise}	β
	$M_\odot$	$R_\odot$			ks	ks	10^{30} erg/s	10^{54} cm^{-3}	MK	MK	$R_\odot$	$R_\odot$	
(1)	(2)	(3)	(4)	(5)	(6)	(7)	(8)	(9)	(10)	(11)	(12)	(13)	(14)
1 053525.73-050949.3_1	0.9	1.8	-1.6	F	1.5 ± 0.3	6.1 ± 1.5	20	1.5	89	55	1.3	1.0	0.03
2 053515.79-053312.0_1	0.3	1.8	-1.4	F	6.6 ± 2.3	30.3 ± 11.0	11	1.3	31	22	2.4	1.7	0.05
3 053515.91-051458.8_1	0.3	2.1	-2.3	F	4.1 ± 0.8	10.9 ± 1.1	80	6.7	59	38	1.7	1.9	0.06
4 034359.68+321402.7_1	0.5	1.5	-2.4	F	1.5 ± 0.2	9.9 ± 1.7	37	3.5	53	28	1.5	1.1	0.07
5 053447.62-054350.7_1	0.6	1.7	-2.9	F	13.5 ± 11.8	20.0 ± 14.3	8	0.9	21	17	1.4	1.8	0.08
6 054703.96+001114.0_1	0.5	1.8	-1.2	F	6.7 ± 1.5	12.3 ± 1.2	43	4.0	136	29	1.4	· · ·	0.09
7 034432.73+320837.3_2	1.2	2.1	-2.4	F	6.0 ± 1.7	6.8 ± 2.5	14	1.5	29	23	0.6	1.1	0.11

55個のフレアについてカタログを作成

結果

フレアの性質は，円盤のあるなしと相関がない

円盤なし　円盤あり

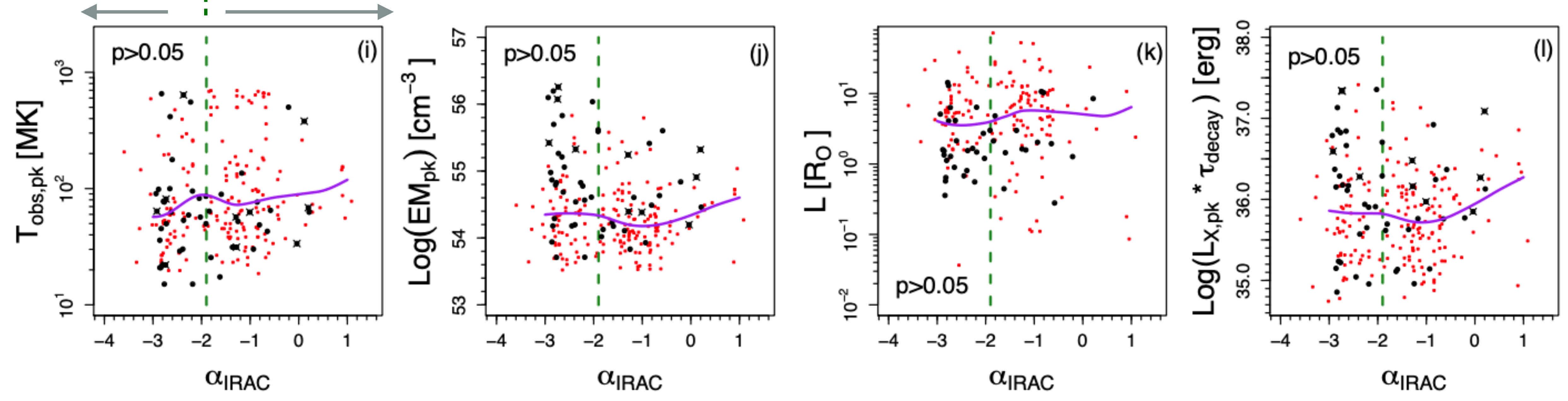

Figure 6. Bivariate scatterplots of several properties of the 55 bright MYStIX/SFiNCs flares (black points) with comparison to the COUP X-ray flares (Getman et al. 2008a,b, red points). Black × symbols represent lower limits for flares that were not fully captured in the MYStIX/SFiNCs exposures. Local regression fits (Loader 2020) are shown as magenta curves. Dashed vertical lines in the bottom panels denote the chosen boundary between disk-bearing (right) and diskless (left) stars. Legends give p-values from Kendall's τ bivariate nonparametric correlation test. Panel descriptions: (a) Flare rise versus decay timescales. (b) Observed peak flare temperature versus decay timescale. (c,d,e,f) Peak flare emission measure, peak flare temperature, flare loop height, flare loop height normalized by stellar radius as functions of stellar mass. (g,h) Flare energy as a function of stellar mass and peak flare temperature. (i,j,k,l) Peak flare temperature, peak flare emission measure, flare loop height, and flare energy as functions of infrared spectral energy distribution slope α_{IRAC}.

フレアの性質は，星の質量と相関がある.

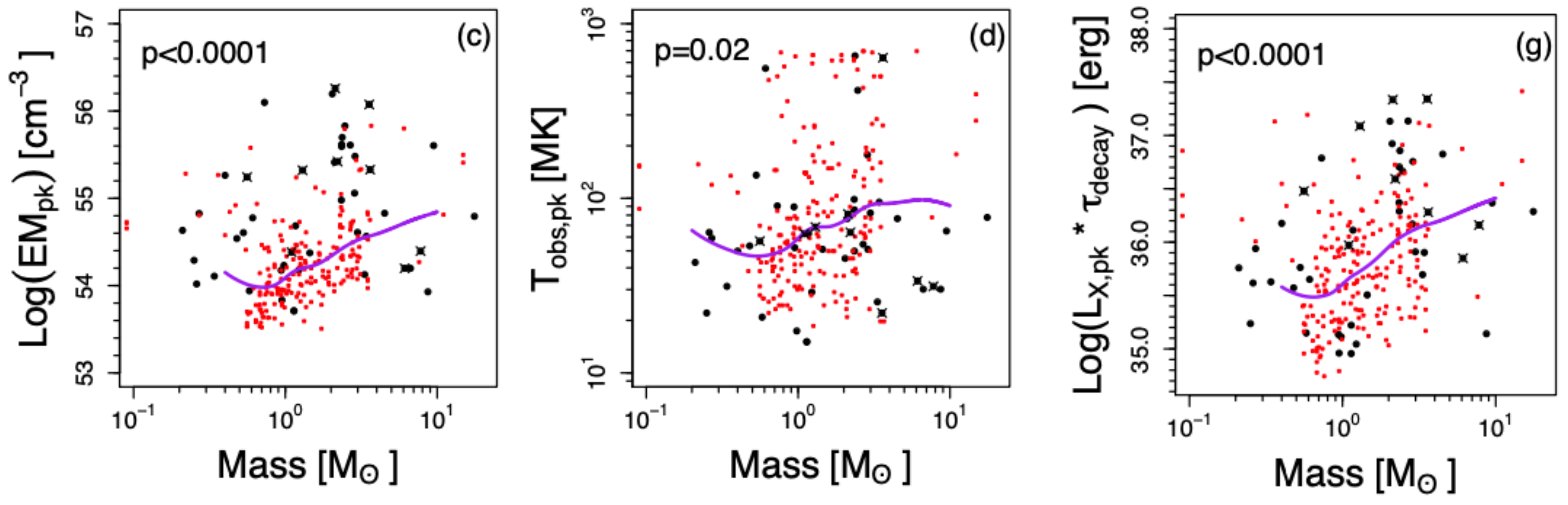

磁束とフレア光度の相関

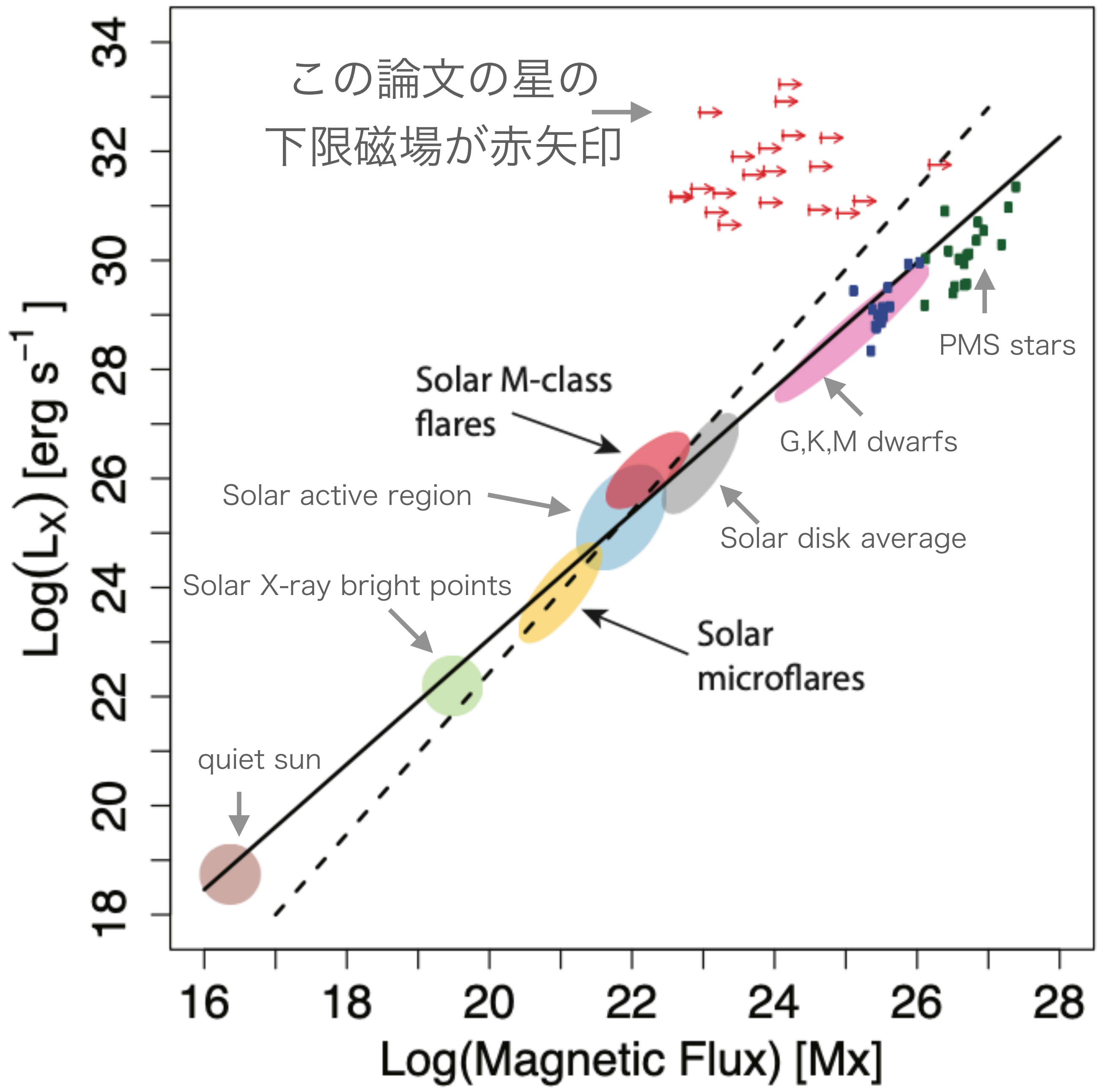

Figure 8. X-ray luminosity as a function of magnetic flux. Lower limits on the magnetic flux for our bright MYStIX/SFiNCs super-flares with available information on loop geometries and stellar radii are indicated by the red arrows. The solid and dashed black lines are the relations $L_X \propto \Phi^m$ with $m = 1.15$ (Pevtsov et al. 2003) and $m = 1.48$ (Kirichenko & Bogachev 2017), respectively. These lines fit various magnetic elements emitting X-rays. From Pevtsov et al. (2003), these include the quiet Sun (brown), solar X-ray bright points (light green), solar active regions (cyan), solar disk averages (grey), and old G, K, M dwarfs (magenta). Solar microflares (golden oval) are from Kirichenko & Bogachev (2017) and solar M-class flares (red oval) are from Su et al. (2007). Individual solar-type dwarfs (blue points) are from Kochukhov et al. (2020). Individual Orion and Taurus PMS stars (dark green points) are from Sokal et al. (2020).

(2) 10. The Macroporosity of Rubble Pile Asteroid Ryugu and Implications for the Origin of Chondrules

William Herbst, James P. Greenwood, Teng Ee Yap

◆小惑星リュウグウのmicroporosity（空間率）を調べた.

◆リュウグウ表面の岩石の大きさ分布から，リュウグウがそのような粒状の集合体と仮定して求める.

空間率 $\phi = 0.14 \pm 0.04$

◆リュウグウの平均密度1.19 g/cm^3 →リュウグウの岩石の密度 1.38 g/cm^3

⬇

◆リュウグウでは，地球上の隕石にある高密度のコンドリュールを含む岩石は，ほとんどない. （コンドリュール：3.0-3.2 g/cm^3）

◆コンドリュールは太陽系全体に分布しているのではなく，局所的に生成されたのではないか.

◆コンドリュールの起源は，溶融している大型小惑星に微惑星が降着する過程で形成されたのではないか.

小惑星リュウグウ （JAXA）

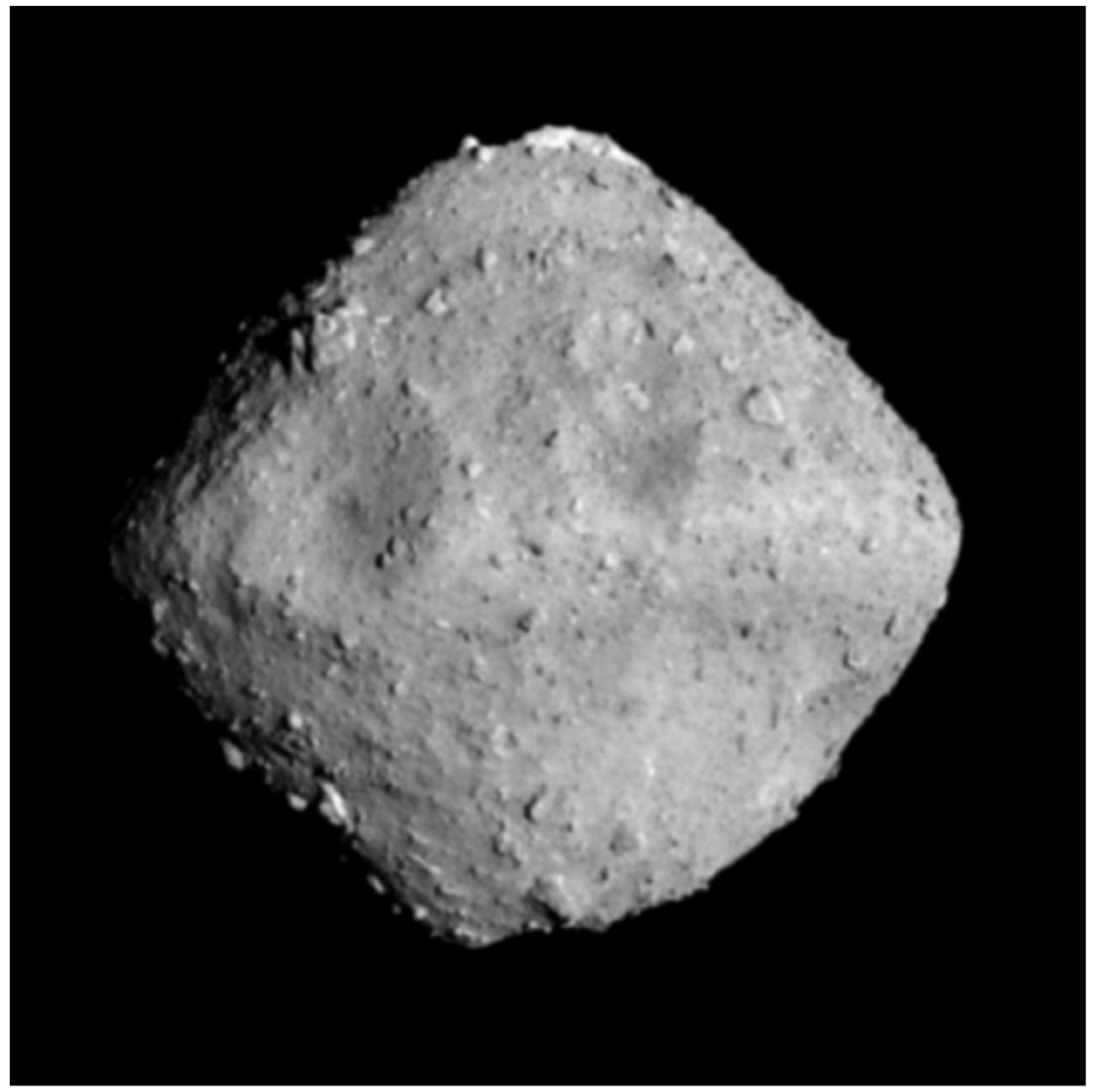

方法と結果

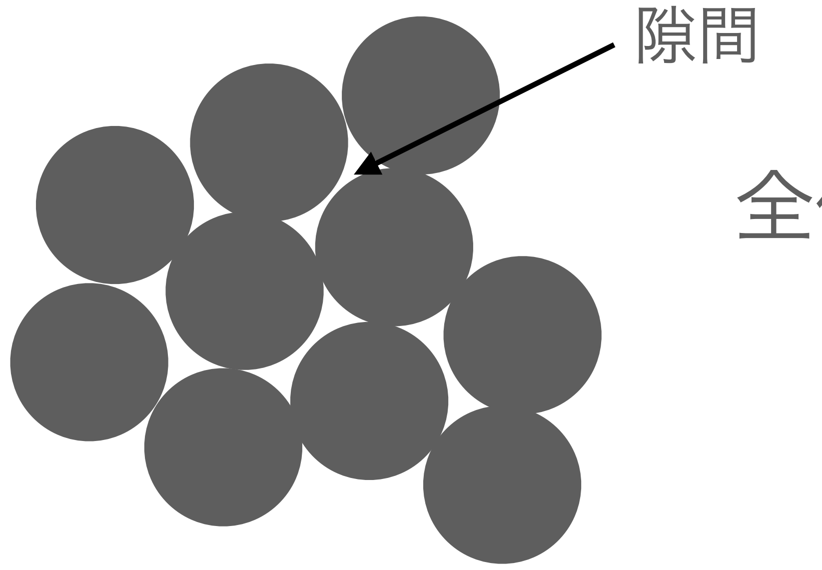

全体積に占める隙間の割合：空間率

同一半径の球の場合：空間率＝0.26（理想的な下限値）

半径が異なる場合
大きな粒子のすきまに小さな粒子が入り，空間率が下がる

サイズ分布がわかると，空間率が推定できそうな気が．．．

リュウグウ表面の岩石のサイズ分布

lognormal 分布 $f(x) = \frac{1}{\sigma x\sqrt{2\pi}} \exp\left(-\frac{(ln(x)-\mu)^2}{2\sigma^2}\right).$

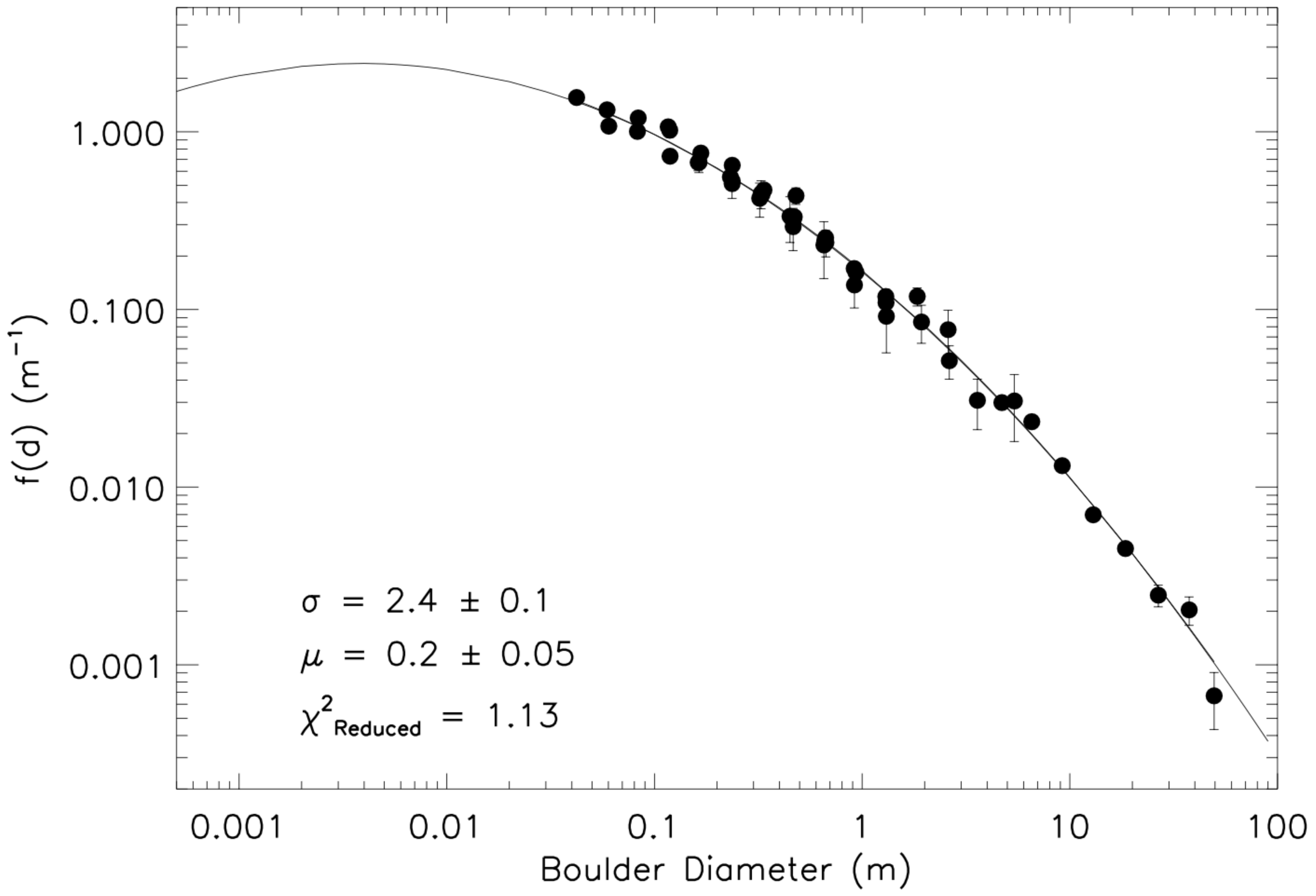

Figure 1. The normalized volume frequency distribution for Ryugu boulders, derived from the areal counts of Michikami et al. (2019), compared to a lognormal distribution with $\sigma = 2.4 \pm 0.1$ and $\mu = 0.2 \pm 0.05$. The fit is clearly quite good and characterized by a reduced $\chi^2 = 1.13$. Error bars based on counting statistics alone are shown. Where they do not appear, the error bars are smaller than the data points.

上のサイズ分布の観測結果と，空間率を推定する理論を用いて，
リュウグウの空間率を求めた．

空間率 $\phi = 0.14 \pm 0.04$

リュウグウの平均密度1.19 g/cm^3 →リュウグウの岩石の密度 1.38 g/cm^3

空間率から求めたリュウグウの密度と，石質隕石の密度との比較

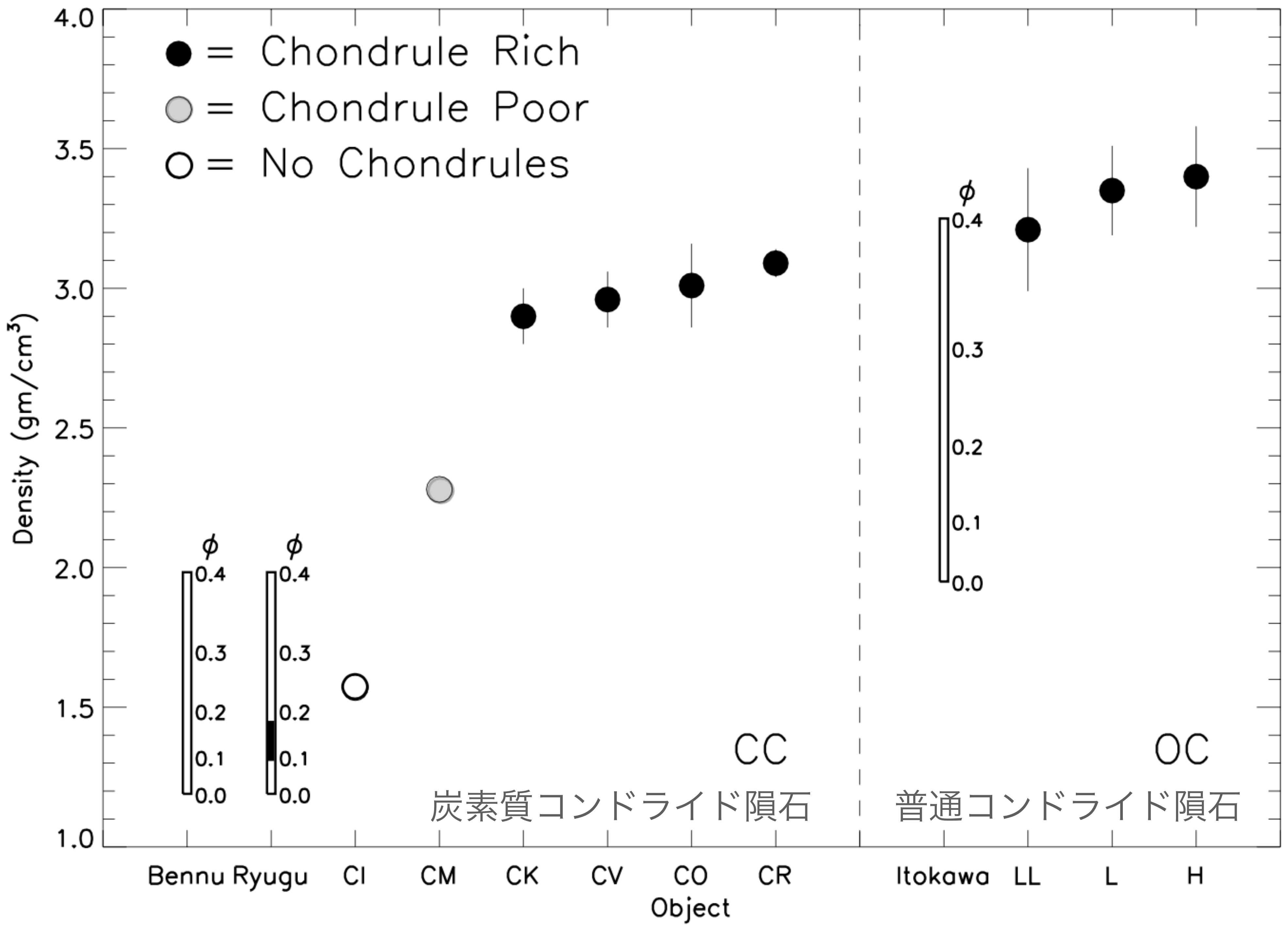

Figure 4. The density of some classes of carbonaceous chondrites (CC) and ordinary chodrites (OC) from Macke, Consolmagno & Britt (2011) are compared to the average density of rocks on three rubble pile asteroids as a function of their macroporosity (ϕ; open bars). The result from this study that $\phi = 0.14 \pm 0.04$ is indicated by the solid portion of Ryugu's bar and corresponds to a density for its rocks of 1.38 ± 0.07.

リュウグウを構成している岩石の密度は，地球上にある石質隕石の密度よりも小さい

リュウグウにはコンドリュール（平均密度が3.0-3.2 g/cm^3）はあまり含まれていない.

議論

コンドリュールは太陽系全体に分布しているのではなく，局所的に生成されたのではないか.

(3) 12. **ALMA observations of doubly deuterated water: Inheritance of water from the prestellar environment**

S. S. Jensen, J. K. Jørgensen, L. E. Kristensen, A. Coutens, E. F. van Dishoeck, K. Furuya, D. Harsono, M. V. Persson

◆水分子がどこでできたのか？

◆クラス0天体（B335とL483)の暖かいエンベロープ（～100K）において，D_2Oの柱密度をALMAで観測し，重水素の割合を調べた.

⬇

◆D_2O/HDO の比が HDO/H_2Oの比の2倍以上だった．この結果は，水分子が星形成前の分子雲の中で形成されたとするモデルと矛盾しない．一方，水分子が原始惑星系円盤で形成されたとすると矛盾する.

◆今回観測した孤立した原始星のHDO/H_2Oの比が，クラスターの中にある原始星の値よりも大きかった．これは，孤立した原始星のほうが，より時間をかけて形成された結果か？

背景と方法

著者の考えている描像

低温の分子雲では重水素の割合が高くなる

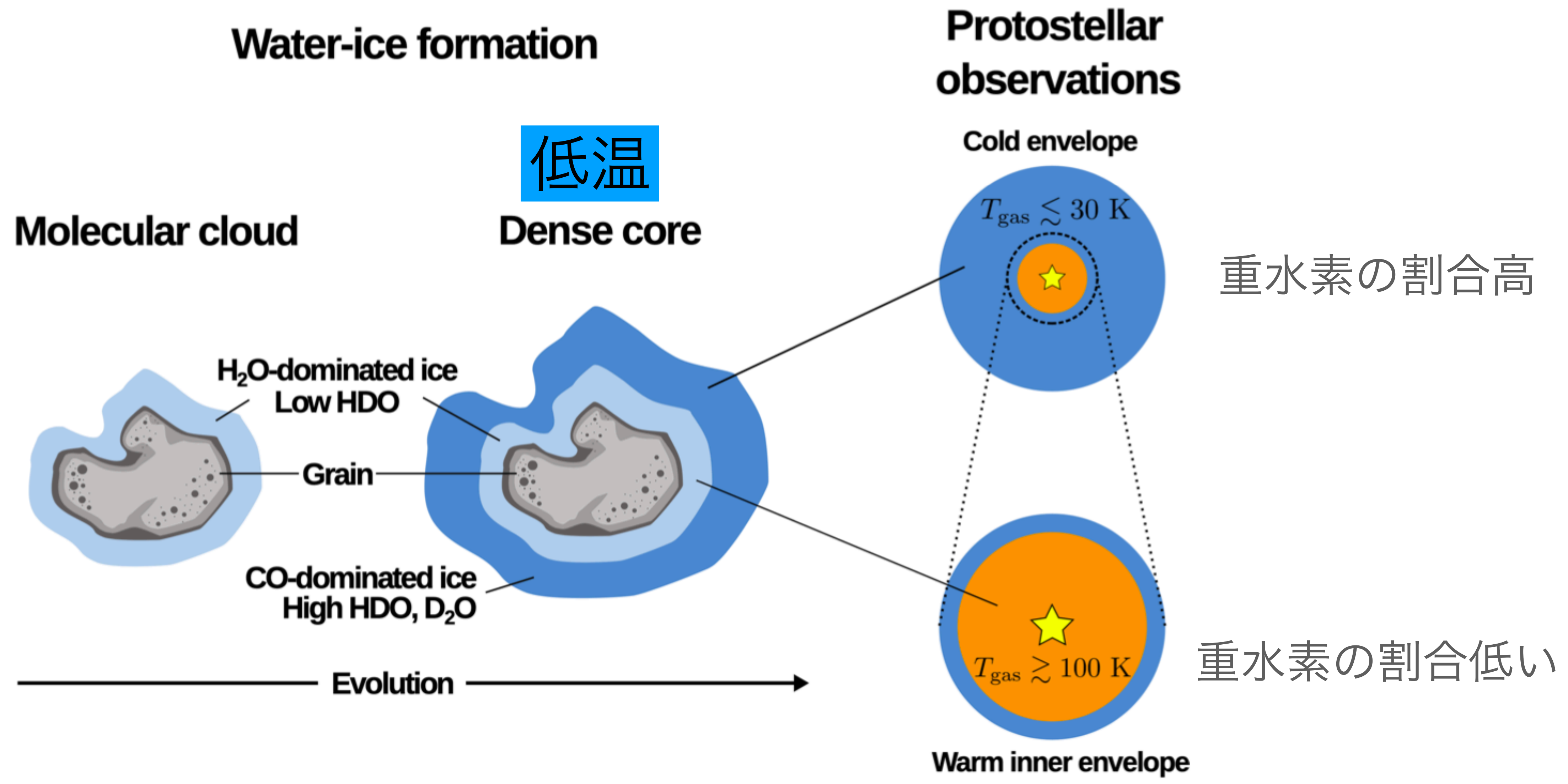

Fig. 1. Schematics of the predicted ice structure in the prestellar core stage (left) and the observed water deuterium fractionation toward embedded low-mass protostars (right). The outer layer of the ice mantle, which has high water D/H ratio, may stem from nonthermal desorption in the cold envelope or cold gas-phase formation. Meanwhile, the whole mantle is sublimated in the hot corino, lowering the HDO/H_2O ratio. The schematical structure is proposed by Furuya et al. (2016). The figure is adopted from van Dishoeck et al. (2021)..

$$H_3^+ + HD \rightleftharpoons H_2D^+ + H_2 + \Delta E$$

逆反応が吸熱．低温で逆反応は阻害される．

H_2D^+が自由電子と解離再結合して原子Dを形成することで、気相では局所的な原子D/H比が上昇．最終的にダスト粒子表面での水素化により，水やその他の分子が生成される。

一方，原始惑星系円盤に含まれる水が、どの程度、星雲から受け継いだものなのか、それとも円盤内で局所的に合成されたものなのか？

結果

クラス0天体（B335とL483)の暖かいエンベロープ（〜100K）

具体的なスペクトルの例

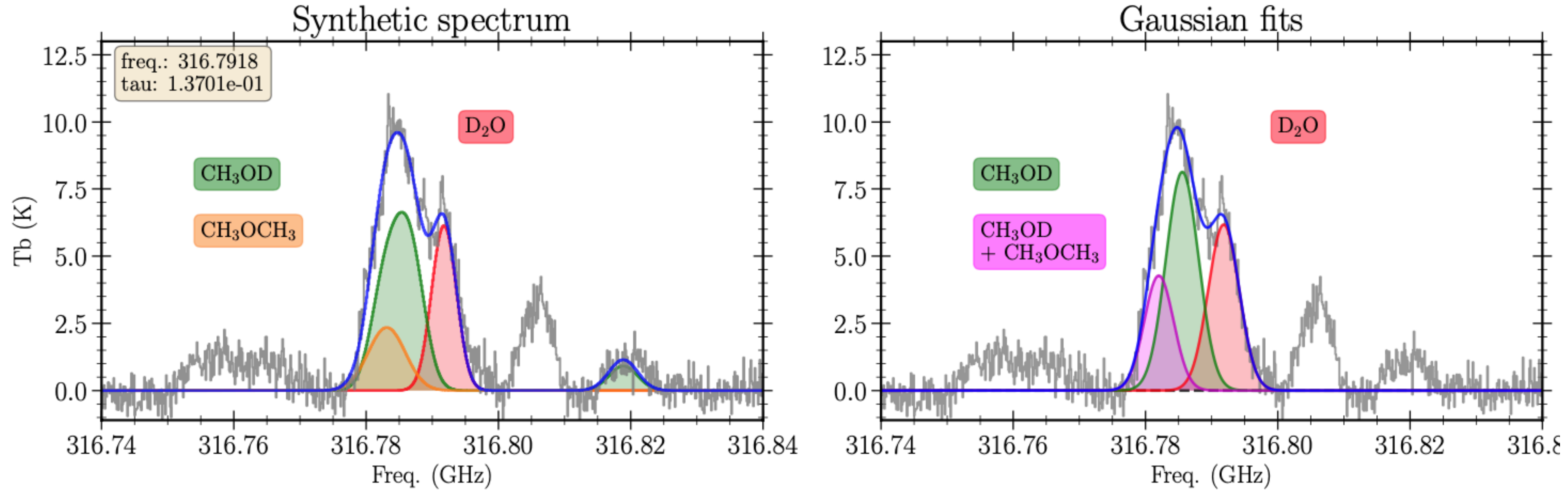

Fig. 4. Overview of the two methods used to determine the column density of D_2O toward B335. *Left*) Synthetic spectrum model for the emissic feature toward B335 for an assumed source size of 0.″2. The estimated optical depth τ for D_2O is shown in the upper left corner. The synthet spectrum includes components from D_2O, CH_3OD, and CH_3OCH_3. *Right*) Least-squares fit to the emission profile. The best fit includes thr Gaussian components, one identified as D_2O, one identified as CH_3OD at 316.7651 GHz, and a third component that may be either CH_3OD 316.7916 GHz or CH_3OCH_3 at 316.7904 GHz, or a convolution of both.

得られた柱密度

Table 2. Overview of the column densities for D_2O, HDO, and $H_2^{18}O$ derived with the best-fit synthetic spectrum model (N_{model}) and with the fitted Gaussian profiles (N_{fit}). The reported full width at half maximum (FWHM) and v_{LSR} are for the synthetic spectrum model. A source size of 0.″2 is assumed for both sources for all molecules.

Molecule	N_{model} (cm^{-2})	N_{fit} (cm^{-2})	FWHM (km/s)	v_{LSR} (km/s)	T_{ex} (K)
		L483			
D_2O	1.1×10^{15}	1.7×10^{15}	(4.5, 5.2)	(1.75, 7.65)	165
HDO	1.1×10^{17}	1.2×10^{17}	(4.9, 5.7)	(1.75, 7.65)	165
$H_2^{18}O$	5.1×10^{16}	5.9×10^{16}	(6.2, 7.1)	(1.75, 7.65)	165
		B335			
D_2O	3.5×10^{15}	4.0×10^{15}	4.25	7.6	220
HDO	2.5×10^{17}	1.9×10^{17}	4.0	7.9	220
$H_2^{18}O$	6.3×10^{16}	7.1×10^{16}	5.65	7.9	220

Table 3. Overview of the D/H ratios of water in the warm region ($\lesssim$ 100 au, $T \gtrsim$ 100 K) toward Class 0 protostars. For L483 and B335, the reported values are derived from the synthetic spectrum model.

Object	f_{D1} HDO/H_2O ($\times10^{-4}$)	f_{D2} D_2O/HDO ($\times10^{-2}$)	f_{D2}/f_{D1}	Reference
		Clustered protostars		
NGC1333 IRAS 2A	7.4 ± 2.1	...	...	1
–	17 ± 8	1.2 ± 0.5	7 ± 4	2
NGC1333 IRAS 4A-NW	5.4 ± 1.5	...	...	1,3
NGC1333 IRAS 4B	5.9 ± 2.6	...	...	1
IRAS 16293–2422	9.2 ± 2.6	...	...	1
		Isolated protostars		
BHR71–IRS1	18 ± 4	...	...	3
B335	17 ± 3	...	...	3
–	63 ± 15	1.4 ± 0.1	2.2 ± 0.5	4
L483	22 ± 4	...	...	3
–	40 ± 5	1.0 ± 0.2	2.5 ± 0.3	4

本研究

Notes. The table only include interferometric observations of the inner warm region toward low-mass Class 0 protostars.

References. (1) Persson et al. (2014); (2) Coutens et al. (2014); (3) Jensen et al. (2019); (4) This work.

fD2/fD1〜2

星形成前の分子雲の中で形成されたとするモデルと矛盾しない.
一方，水分子が原始惑星系円盤で形成されたとすると，この値がもっと小さくなるはず（Furuya et al. 2017).

さらに，B335やL483（孤立した原始星）は，クラスターの中にある原始星に比べて，HDO/H2Oの比が大きい.

8. SIRIUS Project. III. Star-by-star simulations of star cluster formation using a direct N-body integrator with stellar feedback

Michiko S. Fujii, Takayuki R. Saitoh, Yutaka Hirai, Long Wang

One of the computational challenges of cluster formation simulations is resolving individual stars and simulating massive clusters with masses of more than $10^4 M_\odot$ without gravitational softening. Combining direct N-body code with smoothed-particle hydrodynamics (SPH) code, we have developed a new code, ASURA+BRIDGE, in which we can integrate stellar particles without softening. We add a feedback model for HII regions into this code, in which thermal and momentum feedback is given within the Strömgren radius. We perform N-body/SPH simulations of star cluster formation. Without softening, a portion of massive stars are ejected from the forming clusters. As a result, the stellar feedback works outside the clusters. This enhances/suppresses the star formation in initially sub-virial/super-virial clouds. We find that the formed star clusters are denser than currently observed open clusters, but the mass–density relation is consistent with or even higher than that is estimated as an initial cluster density. We also find that some clusters have multiple peaks in their stellar age distribution as a consequence of their hierarchical formation.

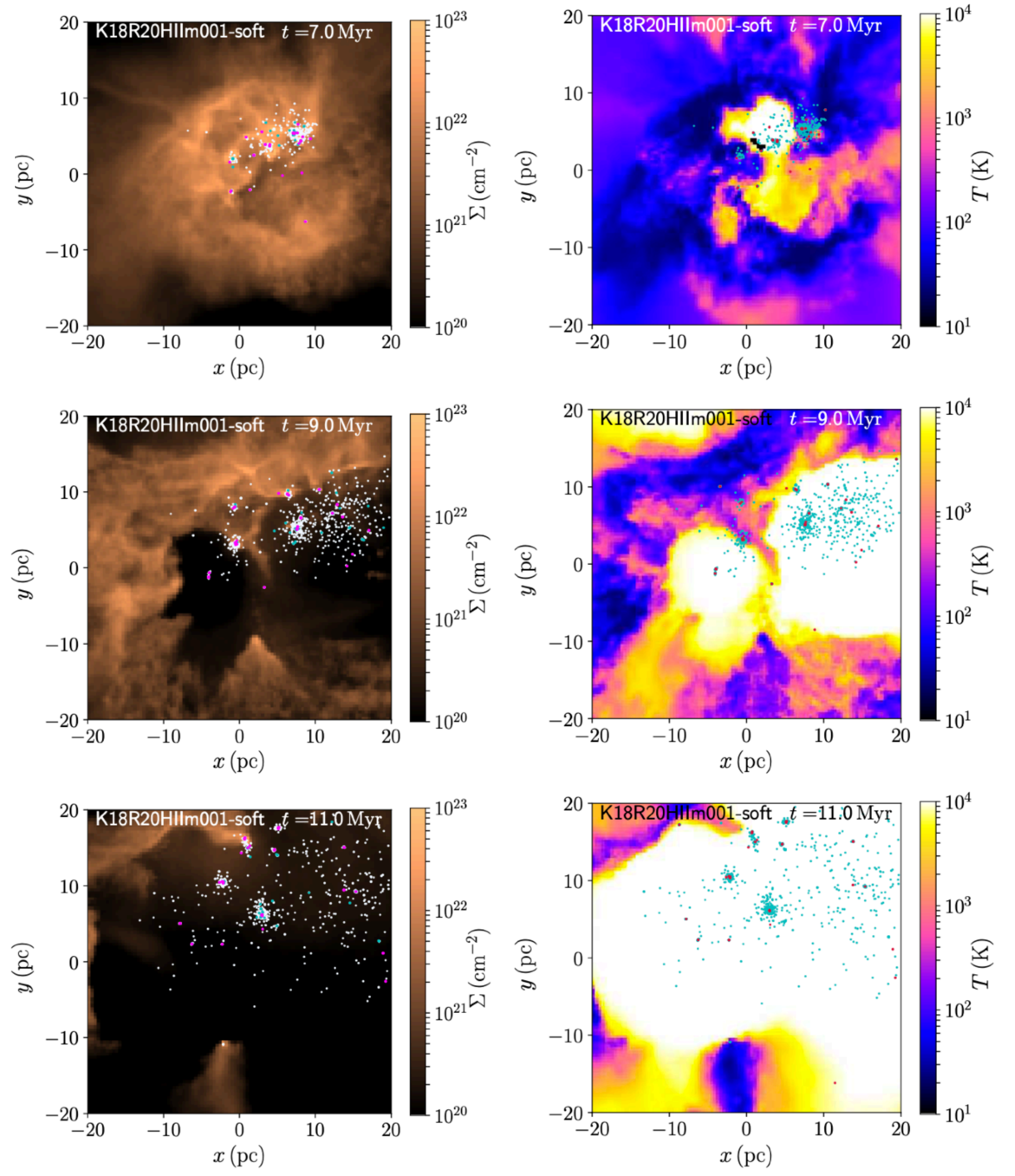

Fig. 4. Time evolution of the distribution of gas and stars for models K18R20m001HII-soft. Left: white, blue, and magenta dots indicate stars with masses of 1–8, 8–20, and $> 20M_\odot$. Color scale indicates gas surface density. Right: blue and red dots indicate stars with masses of 1–20 and $> 20M_\odot$, respectively. Color scale indicates the gas temperature.

11. Misaligned Circumstellar Disks and Orbital Motion of the Young Binary XZ Tau

Takanori Ichikawa, Miyu Kido, Daisuke Takaishi, Yoshito Shimajiri, Yusuke Tsukamoto, Shigehisa Takakuwa

We report our analyses of the multi-epoch (2015-2017) ALMA archival data of the Class II binary system XZ Tau at Bands 3, 4 and 6. The millimeter dust continuum images show compact, unresolved (r < 15 au) circumstellar disks (CSDs) around the individual binary stars; XZ Tau A and B, with a projected separation of 39 au. The 12CO (2-1) emission associated with those CSDs traces the Keplerian rotations, whose rotational axes are misaligned with each other (P.A. -5 deg for XZ Tau A and 130 deg for XZ Tau B). The similar systemic velocities of the two CSDs (VLSR 6.0 km s-1) suggest that the orbital plane of the binary stars is close to the plane of the sky. From the multi-epoch ALMA data, we have also identified the relative orbital motion of the binary. Along with the previous NIR data, we found that the elliptical orbit (e = 0.742+0.025-0.034, a = 0".172+0".002-0".003, and ω = -54.2+2.0-4.7 deg) is preferable to the circular orbit. Our results suggest that the two CSDs and the orbital plane of the XZ Tau system are all misaligned with each other, and possible mechanisms to produce such a configuration are discussed. Our analyses of the multi-epoch ALMA archival data demonstrate the feasibility of time-domain science with ALMA.

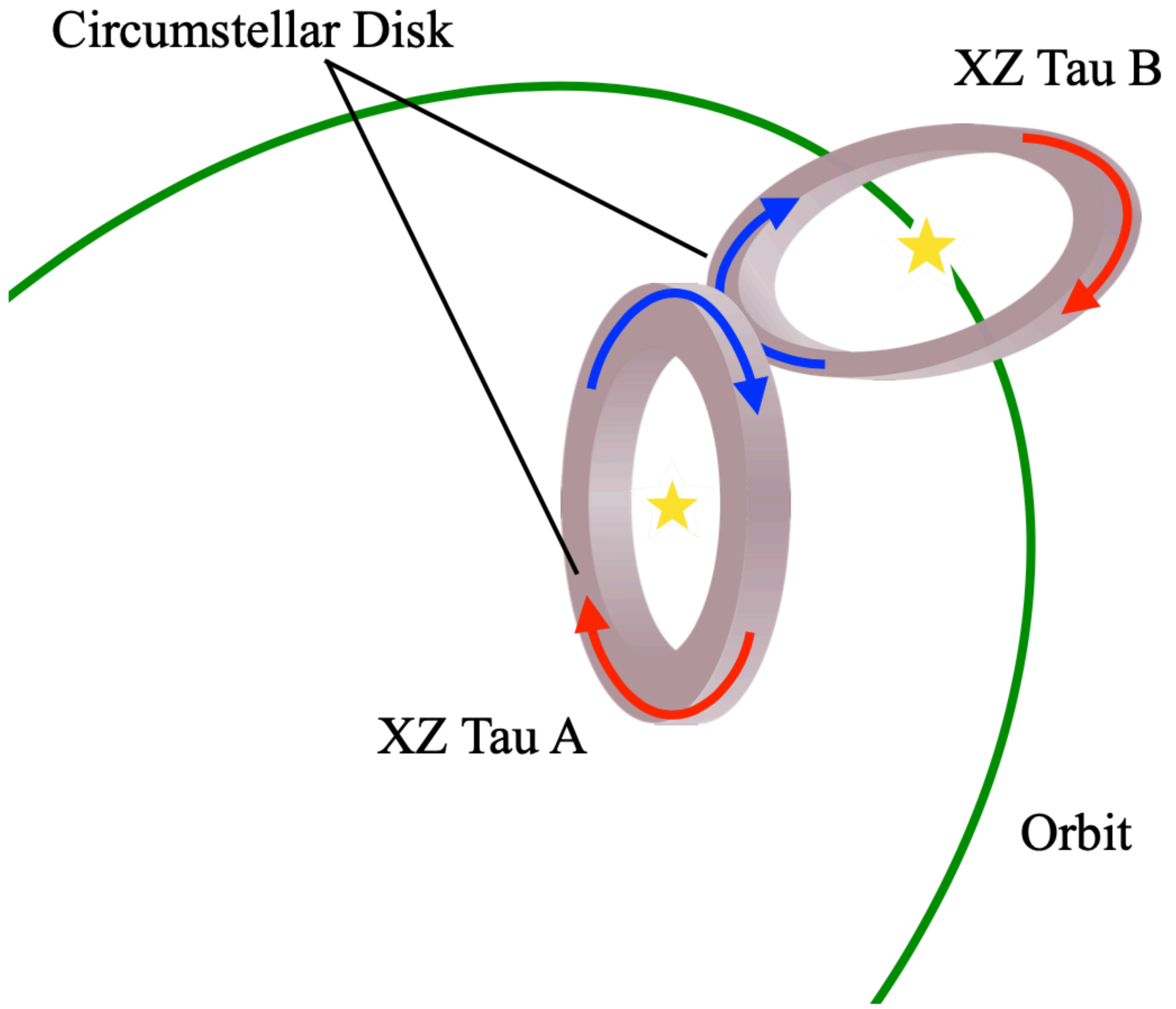

Figure 11. Schematic picture of the binary system XZ Tau revealed by the present ALMA observations.

13. A Deep Search for Five Molecules in the 49 Ceti Debris Disk

Jessica Klusmeyer, A. Meredith Hughes, Luca Matra, Kevin Flaherty, Agnes Kospal, Attila Moor, Aki Roberge, Karin Oberg, Aaron Boley, Jacob White, David Wilner, Peter Abraham

Surprisingly strong CO emission has been observed from more than a dozen debris disks around nearby main-sequence stars. The origin of this CO is unclear, in particular whether it is left over from the protoplanetary disk phase or is second-generation material released from collisions between icy bodies like debris dust. The primary unexplored avenue for distinguishing the origin of the material is understanding its molecular composition. Here we present a deep search for five molecules (CN, HCN, HCO+, SiO, and CH3OH) in the debris disk around 49 Ceti. We take advantage of the high sensitivity of the Atacama Large Millimeter/submillimeter Array (ALMA) at Band 7 to integrate for 3.2 hours at modest spatial (1") and spectral (0.8 km/s) resolution. Our search yields stringent upper limits on the flux of all surveyed molecular lines, which imply abundances relative to CO that are orders of magnitude lower than those observed in protoplanetary disks and Solar System comets, and also those predicted in outgassing models of second-generation material. However, if CI shielding is responsible for extending the lifetime of any CO produced in second-generation collisions, as proposed by Kral et al. (2018), then the line ratios do not reflect true ice phase chemical abundances, but rather imply that CO is shielded by its own photodissociation product, CI, but other molecules are rapidly photodissociated by the stellar and interstellar radiation field.

主系列星のデブリ円盤にCOは多いけど,
それ以外の分子は桁違いに少ない？

Table 3. Upper limits (3σ) on molecular gas emission from the 49 Ceti disk

Species	Rest Frequency[a] GHz	Upper Limit $\mathrm{mJy\,km\,s^{-1}}$	Gas Mass $M_\oplus$
CN(3-2)	340.248*	25	$<2.0 \times 10^{-8}$
SiO(8-7)	347.3305	34	$<8.3 \times 10^{-9}$
HCN(4-3)	354.5054	31	$<1.7 \times 10^{-9}$
HCO^+(4-3)	356.7342	37	$<1.3 \times 10^{-9}$
CH_3OH **	350.9051	22	$<1.5 \times 10^{-7}$
CH_3OH ***	358.6058	56	$<7.6 \times 10^{-7}$

*N=3-2, J=7/2-5/2, F=9/2-7/2 **1(1,1)-0(0,0) ***4(1,3)-3(0,3)

[a]https://www.cv.nrao.edu/php/splat/